Research

Authors for correspondence:

M. Nieves

e-mail: m.nieves@keele.ac.uk

A. Kisil

e-mail: anastasia.kisil@manchester.ac.uk

THE ROYAL SOCIETY PUBLISHING

Analytical and numerical study of anti-plane elastic wave scattering in a structured quadrant subjected to a boundary point load

M. Nieves[1], A. Kisil[2] and G. S. Mishuris[3]

[1]School of Computer Science and Mathematics, Keele University, Keele ST5 5BG, UK
[2]Department of Mathematics, University of Manchester, Oxford Road, Manchester M13 9PL, UK
[3]Department of Mathematics, Aberystwyth University, Aberystwyth, Ceredigion SY23 3BZ, UK

MN, 0000-0003-4616-4548; AK, 0000-0001-7652-5880; GSM, 0000-0003-2565-1961

We verify the recently developed method by Kisil (Kisil 2024 *SIAM J. Appl. Math.* **84**, 464–476 (doi: 10.1137/23M1562445)) through its application in the study of the anti-plane dynamic response of an elastic square-cell lattice quadrant having a free lateral boundary that is subjected to a sinusoidal point load. The vertical boundary of the quadrant is assumed to be either fixed or free. The approach adopted utilizes the discrete Fourier transform in both principal lattice directions to reduce the governing equations to a functional equation linking both the bulk and boundary response of the system. For both problems, this functional equation is shown to reduce to scalar Wiener–Hopf equation whose solution can be exploited to determine the full response of the lattice system. The analytical solutions based on the Wiener–Hopf method are also implemented in numerical investigations that demonstrate the lattice response to various positions and frequencies of the load. In particular, this study includes dynamic regimes induced by the load that possess strong anisotropy and shows how the associated waveforms interact with the boundaries of the quadrant.

1. Introduction

The dynamic analysis of structured systems has an important role in many engineering applications and helps to understand the behaviour of a range of stratified systems encountered in, for instance, civil, maritime and aerospace engineering and materials science [1]. In the latter, the notion of a periodic medium is helping to push the creation of new paradigms concerning the development of materials with counterintuitive and useful properties [2]. In this respect, modelling techniques and analytical methods play an essential role in providing quick and accurate descriptions of the behaviour of such materials. Often, these models are concerned with waves that freely propagate within a periodic system that give rich information about the modes the material can support and the corresponding frequencies.

In reality, one needs to also consider how the waves interact with inhomogeneities that break the structure's periodicity. External or internal boundaries and defects are just some examples, but understanding their role in wave scattering and transport is important in real-world applications. In helping to address this, one can study a diverse range of canonical scattering problems involving discrete structures with defects. A particular class of defects that has received much attention in the literature are linear defects that induce abrupt changes into the geometry of the considered structure. The study of these linear defects often leads to canonical problems whose solutions are amenable to the so-called Wiener–Hopf technique [3,4]. As an example, the problem of the interaction of a plane wave with a semi-infinite defect in square-cell lattice is the first case where the Wiener–Hopf technique was used to tackle such canonical scattering problems for a discrete medium [5]. Note that this problem has also been addressed using lattice Green's functions [6].

Since [5], many works have appeared where the Wiener–Hopf technique has been exploited to study wave scattering by linear defects in stratified systems. Some scalar problems focusing on the anti-plane motion of lattice systems include scattering induced by a rigidly constrained defect [7], wave transmission across surface discontinuities and interfaces in a lattice [8,9]. The Wiener–Hopf technique was also utilized to describe the interaction of waves with multiple lattice cracks [10,11] and the scattering of crack face waves by the tip of a crack embedded in a lattice [12]. Furthermore, the approach of [5] has also been extended to understand in-plane wave scattering by an inertial defect in an elastic lattice [13].

The method applied in [5] is analogous to that adopted by Slepyan and co-workers [14,15] that deals with the dynamic fracture of discrete structures and provides insight into how microlevel waves influence multi-scale failure phenomena. Slepyan's approach has also helped to resolve certain questions concerning crack propagation arising from experiments [16]. In the last 20 years, owing to the development of metamaterials, the [14,15] have also initiated a range of studies into the dynamic fracture of various exotic elastic periodic systems due to the application of some remote load. Utilizing the Wiener–Hopf method, the approach of Slepyan enables one to identify all regimes for stable propagating cracks in a considered structure, as well as waves generated by the propagation of these defects. The theory of dynamic lattice fracture has been developed for periodic structures with, e.g. distributed inhomogeneities [17], structured interfaces [18] and inclusions contained between dissimilar lattice media [19–21]. Lattice fracture problems such as these may also be interpreted as wave scattering problems involving moving boundaries. They play an important role in enhancing the sustainability of materials and their resilience to failure [22]. Furthermore, by employing the notion of flexural periodic multistructures and their dynamic response, e.g. [23,24], the approach of [14,15] can provide simplified models of civil engineering systems undergoing failure [25–27].

A distinctive feature of a majority of the aforementioned works when compared with the current article is the use of a single Fourier transform (either continuous or discrete) which is applied due to the geometric nature and periodicity of the problem under consideration. The present article contributes to the associated area by applying a novel method developed in

[1] to treat dynamic problems for lattice systems with multiple boundaries subjected to some prescribed forcing.

The main result of this paper includes the verification of the method of [1] developed to handle functional equations containing three unknown functions. This is carried out through the study of two problems involving the anti-plane wave motion of an elastic square lattice quadrant subjected to boundary point loading. There, following the application of the Fourier transform in the two principal directions connected with the lattice microstructure, we may reduce the problems to functional equations treatable via the theory in [1]. In particular, in each problem the technique of [1] helps to convert the functional equation into a Wiener–Hopf problem for only one unknown and upon deriving its solution we are able to determine the behaviour of the entire lattice system. Furthermore, the method adopted [1] is shown to be efficient in computing the response of the quadrant. This includes low-frequency responses relative to the lattice cut-off frequency, where the lattice motion can be approximated by the solution of the Helmholtz equation (e.g. [15, chapter 11]). Furthermore, atypical dynamic regimes at higher frequencies within the lattice passband can also be computed. They exhibit highly localized waveforms with preferential directionality. We note that in those regimes, one can trace novel effective equations governing the envelopes of such modes via the application of high-frequency homogenization methods that exploit dispersion degeneracies and standing modes [28,29].

The related responses of the lattice quadrants studied here share a connection with the lattice Green's function, studied for a square lattice in [30]. In fact, these responses can be associated with the discrete analogue of the regular part of Green's function. Some recent works in understanding the behaviour of lattice systems subjected to point loading include elastic lattices and strips with gyroscopic features that can support the one-way propagation of surface, interfacial and bulk waves [31–35]. Similarly, in connection with the problems studied here, we also mention a recent advance in [36], where plane wave scattering by a quadrant in a structured system of infinite extent was addressed.

Examples of some numerical computations obtained from the analytical solutions derived in this paper are given in figure 1. This highlights non-trivial waveforms, possessing several wavefronts or represented by highly localized waves, including their generation by the applied load and their scattering from the quadrants' external boundaries. There we show the total displacement related to the complex valued function representing the displacement of each lattice node (in figure 1*a,c*) and the corresponding real parts (in figure 1*b,d*). Further details of the computations are provided in the following text. We note that the periodicity of the structure is essential in the analytic approach here. However, for more complex discrete systems having a microstructure without periodicity, the analysis of their vibration response is possible with methods such as those in [37] that utilize dynamic Green's functions. For continuous systems with microstructure, we refer also to sophisticated numerical algorithms [38,39] based on the *T*-matrix method [40] to model wave scattering by non-periodic arrays of inclusions.

The structure of the article is as follows. In §2, we introduce the structured quadrant and the description of the two problems considered. We first derive the solution to the constrained lattice quadrant whose vertical boundary is clamped in §§3–6. Details concerning the transition from the associated transient formulation of this problem to the steady-state problem considered are given in electronic supplementary material A [41]. In particular, §3 contains the Fourier transform of the equations governing the structure and the derivation of the functional equation having three unknowns. In §4, we apply the method of [1] to derive a Wiener–Hopf equation for one of the transformed functions and the corresponding solution is developed in §5. Some results utilized in tackling this equation are also given in the electronic supplementary material B [41]. The solution to the problem of the constrained quadrant subjected to point loading is presented in §6. Then in §7, we detail the modifications of the theory developed in §§3–6 to enable the solution of the free quadrant subjected to a point load along its boundary. Numerical
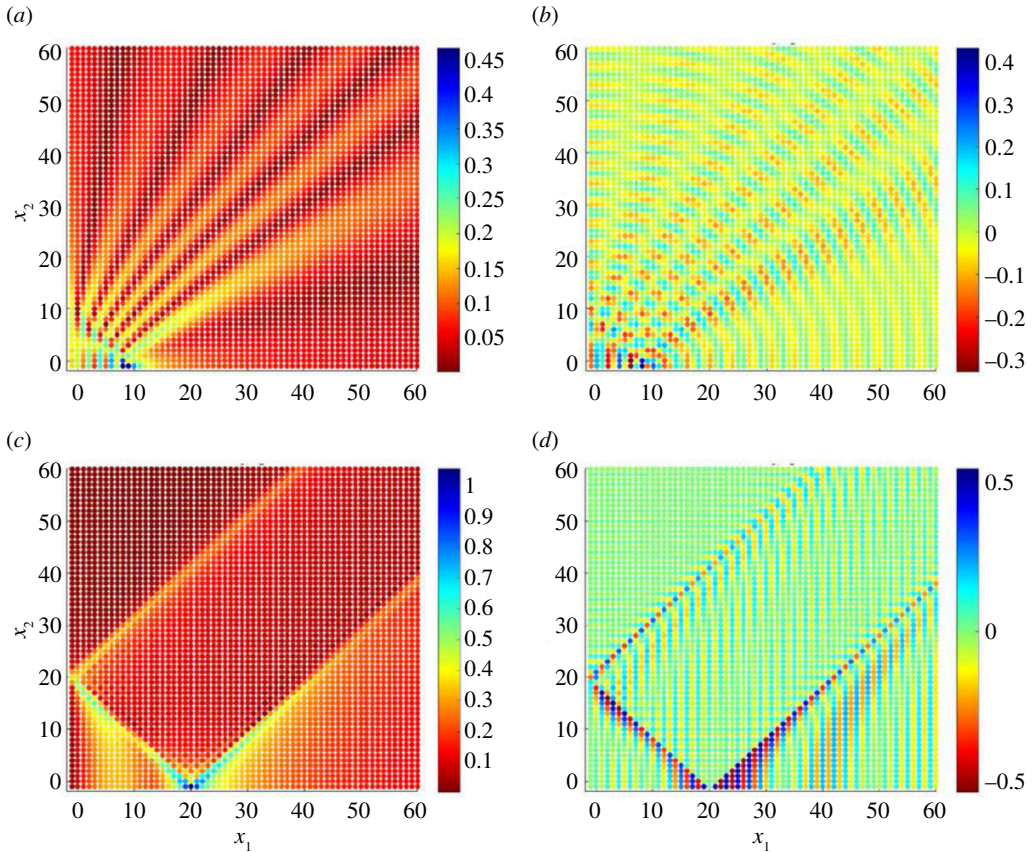
Figure 1. Displacement fields for a lattice quadrant occupying $x_1, x_2 \geq -1$ with a free boundary. (*a,b*) A response of the system created by a point load at $x_1 = 9$, $x_2 = -1$ and frequency 1.5 rad s^{-1}. The total displacement given in (*a*) shows the load creates several regions in the bulk where the displacement is non-neglible. The resulting wave pattern includes waves with several fronts propagating into the bulk of the lattice (see the displacement field in (*b*)). (*c,d*) A highly localized bulk wave mode represented by two rays is created by a combination of the boundary source at $x_1 = 20$, $x_2 = -1$, with frequency 1.99 rad s^{-1}, and the reflection of a localized mode from the left-boundary. The total displacement field in (*c*) shows the localized rays are accompanied by moderate lattice displacements, where some lattice oscillations can be observed in the displacement field in (*d*).

computations corresponding to both problems are then presented in §8, which is then followed by conclusions in §9.

2. Formulation of the problems

We consider the square-cell lattice systems shown in figure 2, composed of elastic links of length L and stiffness $\varkappa$ that interconnect the square array of lattice nodes of mass M. We are concerned with the steady-state motion of these systems that occurs perpendicular to the x_1x_2-plane.

The first lattice quadrant has nodes whose positions are given as $(x_1, x_2) = (Ln_1, Ln_2)$ where $n_1, n_2 \in \mathbb{Z}$, $n_1 \geq -2, n_2 \geq -1$. This lattice possesses nodes along its vertical boundary ($n_1 = -2, n_2 \geq -1$) that are clamped, whereas its lateral boundary at $n_1 > -2, n_2 = -1$, is free to move (see figure 2*a*). The second lattice quadrant has free boundaries, whose nodes will occupy points $(x_1, x_2) = (Ln_1, Ln_2)$, where $n_1, n_2 \in \mathbb{Z}$, $n_1, n_2 \geq -1$ (see figure 2*b*). Later, we show that
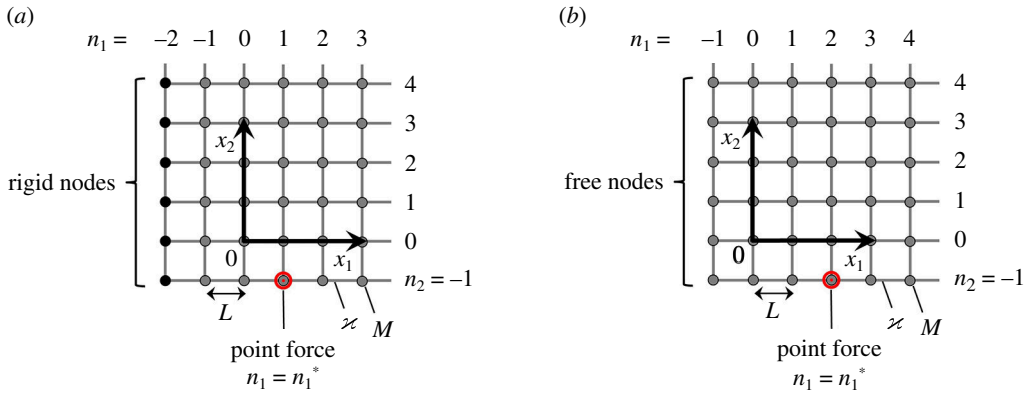
Figure 2. (a) The constrained quadrant located at $x_1 \geq -2L$, $x_2 \geq -L$. The nodes along the boundary corresponding to $n_1 = -2$, $n_2 \geq -1$ are clamped, whereas those on the remaining boundary associated with $n_1 \geq -1$, $n_2 = -1$, are free. (b) The quadrant with a free boundary occupying x_1, $x_2 \geq -L$. The location of the boundary point force in both cases is shown as the red circle and this force acts perpendicularly to the $x_1 x_2$-plane.

for both configurations in figure 2, that we are able to reduce the study to equations associated with nodes contained in n_1, $n_2 \geq -1$. Note that in subsequent sections and all computations discussed in this article, we adopt the normalization described in the next section that corresponds to the case when $L = 1$, i.e., the lattice has links of unit length, as well as unit stiffness, and nodes at the lattice junctions have unit mass.

In both problems, along $n_2 = -1$, a point force with unit amplitude is applied to the node at $n_1 = n_1^*$, with $n_1^* > -1$. This force acts sinusoidally with frequency ω_0 and also perpendicular to the plane in figure 2 (where in this illustration, $n_1^* = 1$). We note that we are interested in the case when the load frequency $\omega_0 < \omega_c = \sqrt{8}$, i.e. the load frequency is contained in the passband for the bulk lattice, with ω_c being the upper limit for this band. In this scenario, the point load can generate waveforms propagating inside the lattice. Mathematically, the response can then be associated with the so-called passband Green's function for the lattice quadrant. Analogously, the case $\omega_0 > \sqrt{8}$ is the stop band Green's function for the quadrant, where the point force generates only localized modes in the vicinity of the load. The phenomenon related to localization effects induced by the point force is not considered here but the analytical derivations given here can also be easily extended to address this type of lattice response.

Going forward, we use the notation $\omega = \omega_0 - i0$ with the right-hand side representing the limit

$$\omega_0 - i0 = \lim_{s \to +0} (\omega_0 - is) \tag{2.1}$$

in accordance with the so-called causality principle [15] (see also electronic supplementary material B [41]). The preceding limit ensures that the functions involved in the transformed equations constructed below remain analytic in an annulus containing the unit circle of $\mathbb{C}$, e.g. see [5].

We will begin by examining the first lattice problem (see figure 2a) in §2a–6, by applying the new method [1]. We then extend this analysis in §7 to solve the second lattice problem (see figure 2b).

Sections 2a–6 also help in providing a better understanding of how we can apply the method of [1] to solve problems involving the lattice quadrant. We note that the problem of figure 2a may also be approached using the method of images, whereby appropriately chosen point forces in a lattice half-plane with a free boundary along $n_2 = -1$ can produce the solution

to the problem involving the constrained quadrant, i.e. one with the vertical boundary being clamped at $n_1 = -2$. The approach is similar to that taken in constructing Green's function for the analogous continuum quadrant, governed by the Helmholtz equation [15] in the interior and with similar mixed boundary conditions along its frontiers (e.g. see [42]). This then reduces the problem to finding the response of the lattice half-plane whose boundary is subjected to a boundary point force. In contrast with the analogous continuum problem, where singular solutions [42] of this type are written in terms of elementary functions, this lattice Green's function [30] is derived in the form of an integral as follows (and similar to [15]). We (i) implement the discrete Fourier transform in the direction parallel to the boundary of the half-plane, (ii) find the transformed bulk half-plane displacements through recurrence relations interconnecting the lattice motion on neighbouring lattice rows, and (iii) ensure the transformed bulk solution satisfies the transformed boundary condition along the half-plane at $n_2 = -1$. The inversion of the Fourier transform then gives the lattice Green's function in the form of a contour integral. Linear combinations of this solution, with appropriate weights, may then be employed to find the function that satisfies the clamped conditions along $n_1 = -2$.

(a) Normalized governing equations for the constrained lattice

From here to §6, we concentrate on the lattice problem associated with figure 2*a*. In this section, we provide the normalized dynamic equations of motion for this problem in the steady-state regime. The normalization adopted in the equations corresponds to a lattice with unit mass at its nodes with unit stiffness for their interconnecting links having a unit length. The equations involve the complex amplitudes of the displacements of the system that satisfy a collection of linear difference equations. The physical system, which is further discussed in electronic supplementary material A [41], is formed from point nodes of a given mass interconnected by linear elastic rods/springs with a uniform stiffness. The anti-plane deformations we study in the quadrant are akin to those encountered in the regime where the point force produces out-of-plane displacements that are small and displacements in the principal directions of the lattice are negligible in comparison. We note that one can also consider material or geometric nonlinearities in the lattice brought by the links and their material properties [43], which can be tackled through the study of the associated Lagrangian of the system.

We use the notation $u_{n_1, n_2} = u(n_1, n_2)$, to represent the dimensionless displacement amplitude of the node associated with the index multi-index $(n_1, n_2) \in \mathbb{Z}^2$, $n_1, n_2 \geq -1$. Note that the dimensionless time-dependent displacements are given by

$$\mathcal{U}(n_1, n_2) = \mathrm{Re}(u_{n_1, n_2} e^{i\omega t}), \quad (n_1, n_2) \in \mathbb{Z}^2, n_1 \geq -2, n_2 \geq -1 .$$

For $n_1, n_2 \geq 0$, the displacement amplitudes u_{n_1, n_2} satisfy

$$u_{n_1, n_2+1} + u_{n_1, n_2-1} + u_{n_1+1, n_2} + u_{n_1-1, n_2} + (\omega^2 - 4) u_{n_1, n_2} = 0, \qquad \text{for } n_1, n_2 \geq 0 . \tag{2.2}$$

Along the boundary associated with $n_1 \geq 0$, $n_2 = -1$, the masses displace according to the equations

$$u_{n_1+1, -1} + u_{n_1, 0} + u_{n_1-1, -1} + (\omega^2 - 3) u_{n_1, -1} = \delta_{n_1, n_1^*}, \qquad \text{for } n_1 \geq 0 , \tag{2.3}$$

with $n_1^* \geq 0$, $n_1^* \in \mathbb{Z}$ representing the location of the point load. The symbol δ_{n_1, n_2} is the Kronecker delta with

$$\delta_{n_1, n_2} = \begin{cases} 1, & \text{if } n_1 = n_2 , \\ 0, & \text{otherwise} , \end{cases}$$

and this has been incorporated into (2.3) to represent the forcing of the node at $n_1 = n_1^*$, $n_2 = 0$.

In addition, for $n_1 = -1$, $n_2 \geq -1$, the node displacements are governed by

$$u_{0,n_2} + u_{-1,n_2+1} + (1 - \delta_{-1,n_2})u_{-1,n_2-1} + (\omega^2 - 4 + \delta_{-1,n_2})u_{-1,n_2} = 0 \tag{2.4}$$

which embeds the condition that the nodes along $n_1 = -2$ are fixed, i.e. $u_{-2,n_2} = 0$, $n_2 \in \mathbb{Z}$ with $n_2 > -1$. Before moving on, we note the analogous equations and quantities governing the lattice in terms of dimensional variables can be obtained through the substitution of

$$\omega = \sqrt{\frac{M}{\varkappa}}\hat{\omega}, \quad t = \sqrt{\frac{\varkappa}{M}}\hat{t}, \quad u_{n_1,n_2} = \frac{\hat{u}_{n_1,n_2}}{L} = \frac{\hat{u}(Ln_1, Ln_2)}{L}, \quad k_j = L\hat{k}_j, \quad j = 1, 2, \tag{2.5}$$

into (2.2)–(2.4), where those variables with the hat on the above right-hand sides carry the appropriate dimensions. Furthermore, in electronic supplementary material A [41], we demonstrate how problems (2.2), (2.3) and (2.4) can be derived from the transient regime, where it is also shown how the small dissipative term that appears with the normalized frequency in these equations.

3. Fourier transform of the governing equations

We demonstrate how the governing equations for the lattice can be reduced to a single functional equation through the application of the discrete Fourier transform with respect to the principal coordinates of the lattice system.

(a) Transformed equations along $n_1 = -1$

In what follows, we use the following notation

$$\Psi_{n_1}^+(y) = \sum_{n_2 \geq 0} u_{n_1,n_2} y^{n_2}, \quad n_1 \geq -1, n_1 \in \mathbb{Z}, \tag{3.1}$$

to represent the transformed solution with respect to the vertical lattice coordinate only.

Adopting (3.1), we multiply (2.4) through by y^{n_2+1} and sum over $n_2 \geq 0$, $n_2 \in \mathbb{Z}$. In using the identities:

$$\sum_{n_2 \geq 0} u_{0,n_2} y^{n_2+1} = y\Psi_0^+(y),$$

$$\sum_{n_2 \geq 0} u_{-1,n_2+1} y^{n_2+1} = \Psi_{-1}^+(y) - u_{-1,0},$$

$$\sum_{n_2 \geq 0} (1 - \delta_{-1,n_2})u_{-1,n_2-1} y^{n_2+1} = y^2[\Psi_{-1}^+(y) + u_{-1,-1}y^{-1}]$$

and

$$\sum_{n_2 \geq 0} (\omega^2 - 4 + \delta_{-1,n_2})u_{-1,n_2} y^{n_1+1} = (\omega^2 - 4)y\Psi_{-1}^+(y)$$

we obtain the equation

$$(y^2 + (\omega^2 - 4)y + 1)\Psi_{-1}^+(y) + y\Psi_0^+(y) - u_{-1,0} + u_{-1,-1}y = 0, \tag{3.2}$$

where $y \in \mathcal{C}_y$ with

$$\mathcal{C}_t := \{t \in \mathbb{C}: |t| = 1\}, \tag{3.3}$$

representing the unit circle in the complex plane associated with y.

(b) Transformed equations along the free boundary

Next, we transform the condition (2.3) and to enable this, we define:

$$\Phi^+_{n_2}(x) = \sum_{n_1 \geq 0} u_{n_1, n_2} x^{n_1}, \quad n_2 \in \mathbb{Z} \text{ with } n_2 \geq -1 . \tag{3.4}$$

Then, we take (2.3), multiply through by x^{n_1+1} and sum the result with respect to $n_1 \geq 0, n_1 \in \mathbb{Z}$. Employing:

$$\sum_{n_1 \geq 0} u_{n_1+1, -1} x^{n_1+1} = \Phi^+_{-1}(x) - u_{0, -1} ,$$

$$\sum_{n_1 \geq 0} u_{n_1, j} x^{n_1+1} = x\Phi^+_j(x) , \quad \text{for} \quad j \geq -1$$

and

$$\sum_{n_1 \geq 0} u_{n_1-1, -1} x^{n_1+1} = x^2 \{\Phi^+_{-1}(x) + u_{-1, -1} x^{-1}\} ,$$

then gives the transformed equation

$$(1 + x^2 + (\omega^2 - 3)x)\Phi^+_{-1}(x) + x\Phi^+_0(x) - u_{0, -1} + u_{-1, -1}x = x^{n_1^*+1} , \tag{3.5}$$

where the right-hand side appears due to the transform of the loading term in (2.3) and $x \in \mathcal{C}_x$.

(c) Transformed equations in the bulk lattice

The final transformed equation we require follows from (2.2). Multiplying this by $x^{n_1+1} y^{n_2+1}$, summing over $n_1, n_2 \in \mathbb{Z}, n_1, n_2 \geq 0$ and utilizing the formulae:

$$\sum_{n_1, n_2 \geq 0} u_{n_1+1, n_2} x^{n_1+1} y^{n_2+1} = y\{U(x, y) - \Psi^+_0(y)\} ,$$

$$\sum_{n_1, n_2 \geq 0} u_{n_1-1, n_2} x^{n_1+1} y^{n_2+1} = xy\{xU(x, y) + \Psi^+_{-1}(y)\}$$

and

$$\sum_{n_1, n_2 \geq 0} u_{n_1, n_2+1} x^{n_1+1} y^{n_2+1} = x\{U(x, y) - \Phi^+_0(y)\} ,$$

$$\sum_{n_1, n_2 \geq 0} u_{n_1, n_2-1} x^{n_1+1} y^{n_2+1} = xy\{yU(x, y) + \Phi^+_{-1}(y)\} ,$$

where

$$U(x, y) = \sum_{n_1, n_2 \geq 0} u_{n_1, n_2} x^{n_1} y^{n_2} ,$$

then gives the transformed equation:

$$A(x, y)U(x, y) - y\Psi^+_0(y) - x\Phi^+_0(x) + xy(\Phi^+_{-1}(x) + \Psi^+_{-1}(y)) = 0 .$$

Here

$$A(x, y) = x + y + x^2 y + y^2 x + (\omega^2 - 4)xy . \tag{3.6}$$

This together with (3.2) and (3.5) then provides the functional equation:

$$A(x,y)U(x,y) + \left[\frac{A(x,y)-y}{x}\right]\Psi^{+}_{-1}(y) + \left[\frac{A(x,y)+x(y-1)}{y}\right]\Phi^{+}_{-1}(x)$$

$$= u_{0,-1} + u_{-1,0} - (x+y)u_{-1,-1} + x^{n^{*}_{1}+1} . \tag{3.7}$$

Employing the condition in (2.4) that embeds the equation governing the behaviour of the corner node of the quadrant for $n_2 = -1$, we also have that the preceding may be written as:

$$A(x,y)U(x,y) + \left[\frac{A(x,y)-y}{x}\right]\Psi^{+}_{-1}(y) + \left[\frac{A(x,y)+x(y-1)}{y}\right]\Phi^{+}_{-1}(x) = F(x,y,n^{*}_{1}), \tag{3.8}$$

for $x \in \mathcal{C}_x$ and $y \in \mathcal{C}_y$, with

$$F(x,y,n^{*}_{1}) = -(x+y+\omega^2-3)u_{-1,-1} + x^{n^{*}_{1}+1} . \tag{3.9}$$

4. Derivation of a Wiener–Hopf equation along the quadrant's free boundary

In this section, we derive the Wiener–Hopf equation for the function $\Phi^{+}_{-1}(x)$ corresponding to the transformed displacements along the free boundary. Beforehand, we discuss some preliminary results required for this.

(a) Dispersion relation and auxiliary results

Next, we consider when

$$A(x,y) = 0 , \tag{4.1}$$

which is the dispersion relation for the bulk medium. The preceding equation yields the dispersion surface governing the appearance of propagating waves in the bulk of the medium, if we set $x = e^{ik_1}$ and $y = e^{ik_2}$ in (4.1) to obtain:

$$\omega^2 = 4 - 2\cos(k_1) - 2\cos(k_2) , \tag{4.2}$$

where in the preceding equation ω, k_1 and k_2 are real quantities. This dispersion surface is shown in figure 3a as a function of the wavenumbers k_j, $j = 1,2$. Furthermore, the selection of ω determines the wavenumbers k_j, $j = 1,2$, where (4.2) is satisfied through the analysis of so-called slowness contours, shown in figure 3b. These contours also embed information about the group velocity of waves and direction of wave propagation in the medium (see also [15]). However, here we deal with the complex transform variables x and $y \in \mathbb{C}$ and roots of (4.1) determine singular features of subsequently transformed functions. Hence, for $\omega = \omega_0 - i0$, solutions $y = y_1$ and y_2 of (4.1) in terms of the variable x can be written as

$$y_1 = P_1(x), \qquad y_2 = P_2(x) , \tag{4.3}$$

with

$$P_1(x) = \frac{\sqrt{f(x)+1} - \sqrt{f(x)-1}}{\sqrt{f(x)+1} + \sqrt{f(x)-1}} , \qquad P_2(x) = \frac{1}{P_1(x)} , \tag{4.4}$$

and $|P_1(x)| < 1$. The notation $\sqrt{\cdot}$ above represents the usual square root with the branch point at the origin and cut located along the negative real axis in $\mathbb{C}$. Additionally,

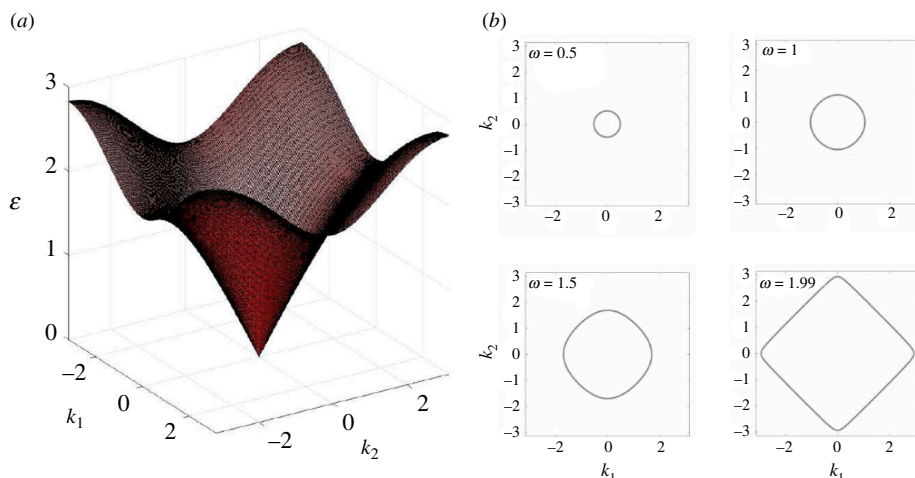$$f(x) = -\frac{1}{2}\left(x + \frac{1}{x} + \omega^2 - 4\right) . \tag{4.5}$$

Figure 3. (a) Dispersion surface based on (4.2) for the bulk lattice in the quadrant and (b) slowness contours corresponding to ω values stated on the inset of the plots.

Similarly, by the symmetry of $A(x, y)$, we can conclude (4.1) also holds when $x = \hat{x}_1$ and $\hat{x}_2$, such that

$$\hat{x}_1 = P_1(y), \qquad \hat{x}_2 = P_2(y) , \tag{4.6}$$

where $|P_1(y)| < 1$. We also exploit these relations in deriving the Wiener–Hopf equation involving the transformed displacements along the free boundary. Finally, we note that owing to (4.3) and (4.6), the function $A(x, y)$ in (4.1) may take the alternate representations:

$$A(x, y) = y(x - P_1(y))(x - P_2(y)) = x(y - P_1(x))(y - P_2(x)) . \tag{4.7}$$

(b) Properties of $P_j(y)$, $j = 1,2$

Note that the function $P_1(y)$ has the asymptotes

$$P_1(y) = -y + (\omega^2 - 4)y^2 + O(y^3) , \qquad \text{as} \quad y \to 0 , \tag{4.8}$$

and

$$P_1(y) = -y^{-1} + (\omega^2 - 4)y^{-2} + O(y^{-3}) , \qquad \text{as} \quad y \to \infty .$$

Similarly, given the interconnection between $P_1(y)$ and $P_2(y)$, we can write

$$P_2(y) = -y^{-1} + 4 - \omega^2 + O(y^2) , \qquad \text{as} \quad y \to 0 ,$$

and

$$P_2(y) = -y + 4 - \omega^2 + O(y^{-2}) \qquad \text{as} \quad y \to \infty .$$

As we consider ω having a small imaginary part, the functions $P_j(y)$, $j = 1,2$ also have branch cuts; each of these functions has one inside and one outside the unit circle $\mathcal{C}_y$. To describe these corresponding branch points, we introduce

$$g_j = (-1)^j + \frac{4 - \omega^2}{2}, \qquad j = 1, 2 .$$

The branch points of $P_j(y)$, $j = 1,2$, are then defined by the following set

10

royalsocietypublishing.org/journal/rspa *Proc. R. Soc. A* **480:** 20240099

11

royalsocietypublishing.org/journal/rspa *Proc. R. Soc. A* **480:** 20240099

$$\mathcal{B} = \mathcal{B}^+ \cup \mathcal{B}^- \tag{4.9}$$

where

$$\mathcal{B}^\pm = \left\{ \frac{\sqrt{g_j + 1} \mp \sqrt{g_j - 1}}{\sqrt{g_j + 1} \pm \sqrt{g_j - 1}}, j = 1, 2 \right\} .$$

The set $\mathcal{B}^+$ ($\mathcal{B}^-$) represents two points connected by a branch cut of $P_j(y)$, $j = 1, 2$, situated inside (outside) the unit circle. To illustrate the branch cuts of $P_1(y)$, we plot $\mathrm{Im}(y)$ using (4.4) in figure 4. There it can be seen that the branch points in (4.9) and associated cuts are either contained inside or outside the unit circle.

(c) A lifted analogue of the transformed bulk equations and the Wiener–Hopf equation

In taking (3.8) and putting $x = P_1(y)$, owing to (4.1), we obtain the so-called lifted equation (see [1]):

$$\Psi_{-1}^+(y) - (P_1(y))^2 (y - 1) y^{-2} \Phi_{-1}^+(P_1(y)) = -P_1(y) y^{-1} F(P_1(y), y, n_1^*) , \tag{4.10}$$

with $y \in \mathcal{C}_y$. Furthermore, setting $x = P_2(y)$ in (3.8) (which can be carried out due to analytical continuation [1]), we obtain

$$\Psi_{-1}^+(y) - (P_2(y))^2 (y - 1) y^{-2} \Phi_{-1}^+(P_2(y)) = -P_2(y) y^{-1} F(P_2(y), y, n_1^*) . \tag{4.11}$$

where $y \in \mathcal{C}_y$.

In both of the preceding equations, y is a continuous variable along the contour $\mathcal{C}_y$. The dependency on Φ_{-1}^+ on y in both equations occurs through two functions ($P_j(y)$, $j = 1,2$). Both functions have branch cuts located on either side of the unit-circle in $\mathbb{C}$. One of these functions takes values inside the unit disk of $\mathbb{C}$, whereas the other takes values outside the unit disk in $\mathbb{C}$. Hence, the second terms on the above left-hand sides are distinct for $y \in \mathcal{C}_y$.

In addition, $\Psi_{-1}^+(y)$ is a continuous function for $y \in \mathcal{C}_y$ as well as being analytic inside this contour and we may use the above equations to eliminate this function. In doing so, subtracting equation (4.10) from (4.11), we have an equation for Φ_{-1}^+ in the form:

$$\begin{aligned} (P_1(y))^2 \Phi_{-1}^+(P_1(y)) - (P_2(y))^2 \Phi_{-1}^+(P_2(y)) \\ = (y - 1)^{-1} y [P_1(y) F(P_1(y), y, n_1^*) - P_2(y) F(P_2(y), y, n_1^*)] , \end{aligned} \tag{4.12}$$

for $y \in \mathcal{C}_y$. Finally, we can map from variable y to variable x by setting $y = P_1(x)$. Noting that

$$P_1(P_1(x)) = x \quad \text{and} \quad P_2(P_1(x)) = x^{-1}$$

allows us to transform (4.12) to the following Wiener–Hopf equation for $\Phi_{-1}^+(x)$

$$x^2 \Phi_{-1}^+(x) - x^{-2} \Phi_{-1}^+(x^{-1}) = x \mathcal{R}(x) - x^{-1} \mathcal{R}(x^{-1}) \tag{4.13}$$

where $x \in \mathcal{C}_x$ and

$$\begin{aligned} \mathcal{R}(x) &= \sigma(x) F(x, P_1(x), n_1^*) \\ &= -((x + \omega^2 - 2)\sigma(x) + \zeta(x)) u_{-1, -1} + x^{n_1^* + 1} \sigma(x) . \end{aligned} \tag{4.14}$$

Here,

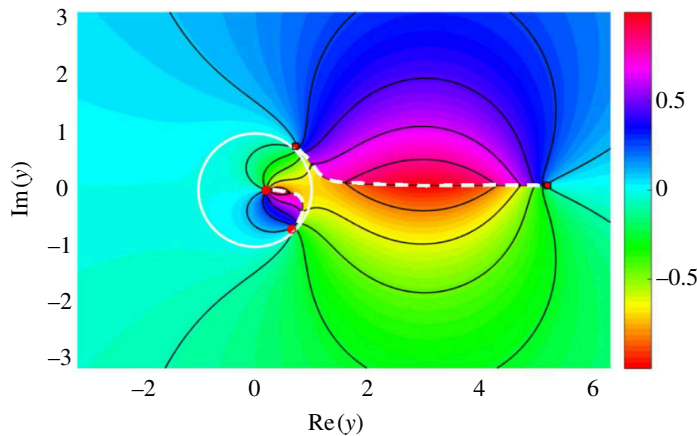$$\sigma(x) = \frac{P_1(x)}{P_1(x) - 1} \quad \text{and} \quad \zeta(x) = P_1(x) .$$

Figure 4. Contour plot of $\text{Im}(P_1(y))$ as a function of the real and imaginary parts of y for the loading frequency $\omega_0 = 0.8$ (such that $\omega = 0.8 - 0.05\text{i}$, see (2.1)). The computations have been performed using (4.4). Branch points of the function defined in (4.9) are shown as red dots inside the unit circle (indicated in white) and by red squares outside this circle. Branch cuts connecting these points are shown by white dashed lines.

5. Solution of the Wiener–Hopf equation

Next, we aim to partition the right-hand side in (4.13) into the sum of two functions, with one function being analytic inside the contour $\mathcal{C}_x$ and the other analytic outside this contour.

(a) The additive split of σ and ζ

First, to perform the required split of (4.13), we need to create the analogous split of the functions $\sigma(x)$ and $\zeta(x)$. Note that these functions have zero index for $x \in \mathcal{C}_x$, which can be proved following similar steps to those presented in [15, chapter 10]. Denoting $p = \sigma$ or ζ, these functions take the representations:

$$p(x) = p_+(x) + p_-(x), \qquad p_\pm = \pm \frac{1}{2\pi\text{i}} \int_{\mathcal{C}_x} \frac{p(\xi)}{\xi - x}\, d\xi, \tag{5.1}$$

where $p_+(x)$ ($p_-(x)$) represents the function that is analytic inside (outside) $\mathcal{C}_x$. Additionally, as $p(x) = p(x^{-1})$, for $p = \sigma$ and ζ (see (4.4) and (4.5)), following the application of the Wiener–Hopf technique, one can show that:

$$p_-(x) = p_+(x^{-1}) - p_+(0), \qquad p = \sigma \text{ and } \zeta. \tag{5.2}$$

(b) Determination of $\Phi_{-1}(x)$ and the displacement of the lattice corner point

Based on §5a, one can check that the Wiener–Hopf equation (4.13) can be written as:

$$x^2\Phi_{-1}^+(x) - x^{-2}\Phi_{-1}^+(x^{-1}) \quad = \quad x\mathcal{N}(x) - x^{-1}\mathcal{N}(x^{-1}) \tag{5.3}$$

for $x \in \mathcal{C}_x$, where

$$\mathcal{N}(x) = -[\mathcal{M}_\sigma^{(1)}(x) + (\omega^2 - 2)\mathcal{M}_\sigma^{(0)}(x) + \mathcal{M}_\zeta^{(0)}(x)]u_{-1,-1} + \mathcal{M}_\sigma^{(n_1^* + 1)}(x). \tag{5.4}$$

Additionally,

$$\mathcal{M}_p^{(n)}(x) = x^n(p_+(x) - p_+(0) + p_0^{(n)}(x^{-1})) - x^{-n-2}[p_+(x) - p_0^{(n+1)}(x)] \,, \tag{5.5}$$

with

$$p_0^{(n)}(x) = \sum_{j=0}^{n} \frac{1}{j!} \frac{\mathrm{d}^j p}{\mathrm{d}x^j}(0) x^j \,, \tag{5.6}$$

for $p = \sigma$ or ζ. The right-hand side in (5.3) now employs the required additive split into two functions, one analytic inside the unit circle $\mathcal{C}_x$ and the other analytic outside this circle. The sketch of the proof of the right-hand side of (5.3) is given in the electronic supplementary material B [41].

We therefore rewrite (5.3) to define:

$$J(x) := Q_+(x) = Q_-(x) \quad \text{for } x \in \mathcal{C}_x \,, \tag{5.7}$$

where

$$Q_+(x) := x^2 \Phi_{-1}^+(x) - x\mathcal{N}(x) \,, \qquad Q_-(x) = x^{-2}\Phi_{-1}^+(x^{-1}) - x^{-1}\mathcal{N}(x^{-1}) \,. $$

We use $Q_+(x)$ $(Q_-(x))$ to extend the definition of $J(x)$ inside (outside) the circle $\mathcal{C}_x$. Note, $\Phi_{-1}^+(x) \to u_{0,-1}$, a bounded quantity, as $x \to 0$ owing to the definition (3.4). Likewise $\Phi_{-1}^+(x^{-1}) \to u_{0,-1}$ as $x \to \infty$. Furthermore, using (5.4), we have that:

$$\mathcal{N}(x) = C_0 + O(x) \,, \qquad x \to 0 \,, \tag{5.8}$$

with C_0 being a constant given as the bounded quantity

$$C_0 = -[\mathcal{M}_\sigma^{(1)}(0) + (\omega^2 - 2)\mathcal{M}_\sigma^{(0)}(0) + \mathcal{M}_\zeta^{(0)}(0)]u_{-1,-1} + \mathcal{M}_\sigma^{(n_1^*+1)}(0) \,, \tag{5.9}$$

where

$$\mathcal{M}_p^{(n)}(0) = \lim_{x \to 0} \mathcal{M}_p^{(n)}(x) \,, \qquad p = \sigma, \zeta \,, \quad \text{for } n \geq 0 \,. $$

We choose $u_{-1,-1}$ in such a way that $C_0 = 0$, requiring that

$$u_{-1,-1} = \frac{\mathcal{M}_\sigma^{(n_1^*+1)}(0)}{\mathcal{M}_\sigma^{(1)}(0) + (\omega^2 - 2)\mathcal{M}_\sigma^{(0)}(0) + \mathcal{M}_\zeta^{(0)}(0)} \,. \tag{5.10}$$

Consequently, both terms in $Q_+(x)$ $(Q_-(x))$ go to zero as $O(x^2)$ $(O(x^{-2}))$ when $x \to 0$ $(x \to \infty)$. Hence, by applying Liouville's theorem, we deduce $J(x) \equiv 0 = Q_-(x) = Q_+(x^{-1})$, leading to

$$\Phi_{-1}^+(x) = \frac{\mathcal{N}(x)}{x} \,, \tag{5.11}$$

whereas we also deduce

$$\Phi_{-1}^+(x^{-1}) = x\mathcal{N}(x) \,. \tag{5.12}$$

Finally, we note that due to the choice of corner point displacement $u_{-1,-1}$ in (5.10) that Φ_{-1}^+ defined through (5.11) remains analytic at $x = 0$.

6. Solution to the problem for a constrained quadrant

(a) Identifying the remaining transformed functions

Having determined $\Phi^+_{-1}(x)$, one can then identify the function $\Psi^+_{-1}(y)$ from the lifted transformed bulk equation (see §4c). Thus we take (4.10) and write

$$\Psi^+_{-1}(y) = P_1(y)(y-1)y^{-2}\mathcal{N}(P_1(y)) - P_1(y)y^{-1}F(P_1(y), y, n^*_1) , \tag{6.1}$$

for $y \in \mathcal{C}_y$, where the right-hand side now utilizes (5.4) owing to (5.11). Furthermore, one can check through the above representation that $\Psi^+_{-1}(y)$ is bounded as $y \to 0$ as a result of (4.8) and (5.8)–(5.10).

In addition, the function $U(x, y)$ representing the transformed bulk displacements in the constrained quadrant $n_1, n_2 \geq 0$ can then be found from (3.8):

$$U(x, y) = - B_\Psi(x, y)\Psi^+_{-1}(y) - B_\Phi(x, y)\Phi^+_{-1}(x) + B_F(x, y, n^*_1) , \tag{6.2}$$

with

$$B_\Phi(x, y) = \frac{1}{y}\left(1 + \frac{(y-1)}{(y - P_1(x))(y - P_2(x))}\right) ,$$

$$B_\Psi(x, y) = \frac{1}{x}\left(1 - \frac{1}{(x - P_1(y))(x - P_2(y))}\right) , \tag{6.3}$$

and

$$B_F(x, y, n^*_1) = \frac{x^{n^*_1 + 1} - (x + y + \omega^2 - 3)u_{-1,-1}}{y(x - P_1(y))(x - P_2(y))} ,$$

owing to the representation of $A(x, y)$ in (4.7).

(b) The lattice displacements

The lattice displacements are then identified through the inversion of the discrete Fourier transform(s). Therefore, the displacements along the free boundary of the quadrant are found from

$$u_{n_1, -1} = \frac{1}{2\pi i}\oint_{\mathcal{C}_x} \Phi^+_{-1}(x)x^{-n_1 - 1}\, \mathrm{d}x , \qquad n_1 \geq 0 , \tag{6.4}$$

with $\Phi_{-1}(x)$ given by (5.11). Similarly, the displacements along the vertical lattice chain at $n_1 = -1$ neighbouring the fixed boundary are obtained from

$$u_{-1, n_2} = \frac{1}{2\pi i}\oint_{\mathcal{C}_y} \Psi^+_{-1}(y)y^{-n_2 - 1}\, \mathrm{d}y , \qquad n_2 \geq 0 , \tag{6.5}$$

with $\Psi^+_{-1}(y)$ taken from (6.1). Completing the description of the lattice quadrant's response along its frontiers is the value of the corner point $u_{-1,-1}$ provided in (5.10).

Finally, the displacements in the quadrant $n_1, n_2 \geq 0$ are found from the double transform inversion applied to $U(x, y)$ in (6.2) as follows:

$$u_{n_1, n_2} = -\frac{1}{4\pi^2}\oint_{\mathcal{C}_y}\oint_{\mathcal{C}_x} U(x, y)x^{-n_1 - 1}y^{-n_2 - 1}\, \mathrm{d}x\mathrm{d}y , \qquad n_1, n_2 \geq 0 . \tag{6.6}$$

7. Unconstrained quadrant subjected to a point force

Having solved the problem of the constrained lattice quadrant subjected to a force along its free boundary (see figure 2b), we now tackle the problem when both boundaries of the quadrant are free to move, with a forced lateral boundary. Below, we detail the modifications to the above method to provide the solution for this problem.

(a) Transformed equations for the quadrant with a free boundary

In this case, in the problem formulation detailed in §§2 and 3, the governing equation (2.4) is replaced with the condition:

$$u_{0,n_2} + u_{-1,n_2+1} + (1 - \delta_{-1,n_2})u_{-1,n_2-1} + (\omega^2 - 3 + \delta_{-1,n_2})u_{-1,n_2} = 0 \tag{7.1}$$

and upon applying the Fourier transform in y in (3.1), we obtain

$$(y^2 + (\omega^2 - 3)y + 1)\Psi_{-1}^+(y) + y\Psi_0^+(y) - u_{-1,0} + u_{-1,-1}y = 0, \tag{7.2}$$

which is derived in an analogous way to (3.5). Now, following the approach of §3c and using (3.5) and (7.2), we can derive a functional equation for the transformed bulk displacements as:

$$A(x,y)U(x,y) + \left[\frac{A(x,y) + y(x-1)}{x}\right]\Psi_{-1}^+(y) + \left[\frac{A(x,y) + x(y-1)}{y}\right]\Phi_{-1}^+(x)$$

$$= \quad G(x,y,n_1^*). \tag{7.3}$$

for $x \in \mathcal{C}_x$ and $y \in \mathcal{C}_y$, with

$$G(x,y,n_1^*) = -(x + y + \omega^2 - 2)u_{-1,-1} + x^{n_1^*+1}, \tag{7.4}$$

that incorporates the transformation of the loading term representing the point load across the lateral boundary.

(b) The Wiener–Hopf equation for the quadrant with a free boundary subjected to a point load

Following analogous steps to §4c, we perform the lift [1] of (7.3) with $x = P_1(y)$ and $P_2(y)$. Using the resulting equations to eliminate the transformed function $\Psi_{-1}^+(y)$, one obtains the Wiener–Hopf equation for $\Phi_{-1}^+(x)$ as:

$$x(1-x)\Phi_{-1}^+(x) - x^{-1}(1 - x^{-1})\Phi_{-1}^+(x^{-1}) \quad = \quad (1-x)\mathcal{S}(x) - (1 - x^{-1})\mathcal{S}(x^{-1}), \tag{7.5}$$

where $x \in \mathcal{C}_x$ and

$$\mathcal{S}(x) \quad = \quad \sigma(x)G(x, P_1(x), n_1^*)$$

$$= \quad -((x + \omega^2 - 1)\sigma(x) + \zeta(x))u_{-1,-1} + x^{n_1^*+1}\sigma(x). \tag{7.6}$$

In the left-hand side (7.5), the first and second terms are analytic inside and outside $\mathcal{C}_x$ and we seek the analogous split of the right-hand side. In achieving this, one obtains:

$$x(1-x)\Phi_{-1}^+(x) - x^{-1}(1 - x^{-1})\Phi_{-1}^+(x^{-1}) = (1-x)\mathcal{T}(x) - (1 - x^{-1})\mathcal{T}(x^{-1}), \tag{7.7}$$

for $x \in \mathcal{C}_x$, with

$$\mathcal{T}(x) = -[\mathcal{Q}_\sigma^{(1)}(x) + (\omega^2 - 1)\mathcal{Q}_\sigma^{(0)}(x) + \mathcal{Q}_\zeta^{(0)}(x)]u_{-1,\,-1} + \mathcal{Q}_\sigma^{(n_1^* + 1)}(x)\,, \qquad (7.8)$$

and

$$\mathcal{Q}_p^{(n)}(x) = x^n(p_+(x) - p_+(0) + p_0^{(n)}(x^{-1})) - x^{-n-1}[p_+(x) - p_0^{(n)}(x)]\,, \qquad (7.9)$$

for $p = \sigma$ and ζ, where (5.6) is also used. The proof of (7.7) follows the same lines as that for (5.3) outlined in the electronic supplementary material B [41] with obvious modifications.

(c) Solution to the transformed problem

The solution to the Wiener–Hopf equation (7.7) then can be obtained in an analogous fashion to §5b, which gives:

$$\Phi_{-1}^+(x) = \frac{\mathcal{T}(x)}{x}\,, \qquad (7.10)$$

where the corner point displacement appearing in (7.8) needs to be chosen as:

$$u_{-1,\,-1} = \frac{\mathcal{Q}_\sigma^{(n_1^* + 1)}(0)}{\mathcal{Q}_\sigma^{(1)}(0) + (\omega^2 - 1)\mathcal{Q}_\sigma^{(0)}(0) + \mathcal{Q}_\zeta^{(0)}(0)}\,. \qquad (7.11)$$

so that the right-hand side of (7.10) remains analytic at $x = 0$. In the above,

$$\mathcal{Q}_p^{(n)}(0) = \lim_{x \to 0} \mathcal{Q}_p^{(n)}(x)\,, \qquad p = \sigma, \zeta\,, \quad \text{for} \quad n \geq 0\,.$$

With (7.10) in hand, we can derive the function $\Psi_{-1}(y)$ from the lifted analogue of (7.3) obtained by setting $x = P_1(y)$, so that:

$$\Psi_{-1}^+(y) = -\frac{P_1(y)(y - 1)}{y^2(P_1(y) - 1)}\mathcal{T}(P_1(y)) + \frac{P_1(y)}{y(P_1(y) - 1)}G(P_1(y), y, n_1^*)\,. \qquad (7.12)$$

Using (7.3), (7.10) and (7.12), we then derive the transformed bulk displacements as:

$$U(x, y) = -B_\Phi(y, x)\Psi_{-1}^+(y) - B_\Phi(x, y)\Phi_{-1}^+(x) + C_F(x, y, n_1^*)\,, \qquad (7.13)$$

with

$$C_F(x, y, n_1^*) = \frac{x^{n_1^* + 1} - (x + y + \omega^2 - 2)u_{-1,\,-1}}{y(x - P_1(y))(x - P_2(y))}\,,$$

and $B_\Phi(x, y)$ is given in (6.3). Finally, we use the inversion formulas (6.4), (6.5) and (6.6) to obtain the displacements for the lattice quadrant with a free boundary subjected to a point force.

8. Numerical illustrations of the lattice response

In this section, we implement the solutions presented in §§6b and 7 in the computation of the quadrant's response to the point load along the free boundary. For a quadrant with either a free boundary or having one side clamped, we also identify unique dynamic responses attributed to the quadrant's underlying microstructure. We focus our study on the case when the point source is chosen to be situated near the quadrant's corner point, where one can observe how the load promotes high stress concentrations and investigate the sensitivity of the form of these concentrations to changes in the loading frequency. Therefore, in this section, we consider the case when $n_1^* = 2$, i.e. the point is situated at $x_1 = 2, x_2 = -1$. Note that in all computations

described here, we adopt the normalization described in §2a, which leads to a lattice with links of unit length and stiffness and nodes with unit mass.

Before continuing, we mention that the results presented here and in §1 have been checked using the governing equations for the medium given in §§2 and 7. In all cases, the computed displacements produce a small error in the governing finite difference equations in the range $O(10^{-3})$ to $O(10^{-4})$, indicating a very high accuracy in the numerical computations shown. The small discrepancy appears naturally due small errors incurred numerically when executing the Wiener–Hopf split required by the solutions and the inversion of the double discrete Fourier transform.

(a) Total displacement of the quadrant microstructure

We begin with analysis of the total displacement of each node in the lattice quadrant. Several plots of the total displacement for the constrained quadrant and the free quadrant are shown in figure 5 for a range of frequencies. The total displacement provides an overall indication of how both the real and imaginary parts of the solutions, given in §§6 and 7c, behave spatially. It also highlights regions of the structure possessing high strain concentrations. In correspondence with this and as expected on physical grounds, figure 5 shows the node loaded by the point forces undergoes a large displacement.

An overall feature in figure 5a,c,e,f is that the displacement in the vicinity in the constrained left-hand boundary is small due to the presence of the clamping conditions. Figure 5b,d,f,h, also show that the quadrant with a free boundary allows high deformations to persist along its vertical boundary as this is free to move and to sustain vibration.

Furthermore, as shown in figure 5, our solution helps to indicate (i) those regions exhibiting strains comparable to those found near the location of the point source, and (ii) the location of such regions and the dependency of their size, shape and number with respect to the loading frequency. All computations shown in figure 5 indicate that the geometry of the region possessing high strains and localized to the quadrant's corner is very distinct. For low frequencies relative to ω_c, a single stress concentration appears in the vicinity of the load (see figure 5a,b). With increase of the loading frequency, it can happen that the concentration can assume several preferential directions that persist in the bulk lattice and their direction depends on the load frequency and boundary conditions of the structure. For example, figure 5c shows there are strain concentrations near the corner which are aligned at approximately 0° and 60°, whereas at a higher loading frequency, figure 5e shows there are concentrations aligned at approximately 0°, 40° and 60°. This effect is linked to the to topology of the slowness contours in figure 3, which at high frequencies relative to ω_c do not possess a circular shape as expected in the low-frequency regime where the structure has an isotropic response.

In particular, for both quadrants considered, the localized stress concentrations dictate the bulk lattice response. They also promote the appearance of regions bounded by inclined rays emanating from the lattice corner point where deformations in the structure can persist. For instance, see figure 5e,f where three such bulk regions exist. Within these regions, the lattice deformations behave like $O(r^{-1/2})$ where r is the radial distance from the corner point (see also [30]). Note that intermediate to these regions, the displacement of the system is small.

Finally, at higher frequencies, the bulk lattice exhibits strong anisotropy in its dynamic response, e.g. see figure 3 where the slowness contours are almost square. In this case, the load produces two highly concentrated modes that propagate at 45° and 135° in the medium. Outside of these rays, the lattice response is small. It is noted that both ray directions are consistent with the group velocity vector associated with the slowness contours [15]. One of the rays is reflected by the left-hand quadrant boundary and propagates parallel to the ray travelling at 45° relative to the positive x_1-axis from the point load. It is noted for the case of the free quadrant, the total
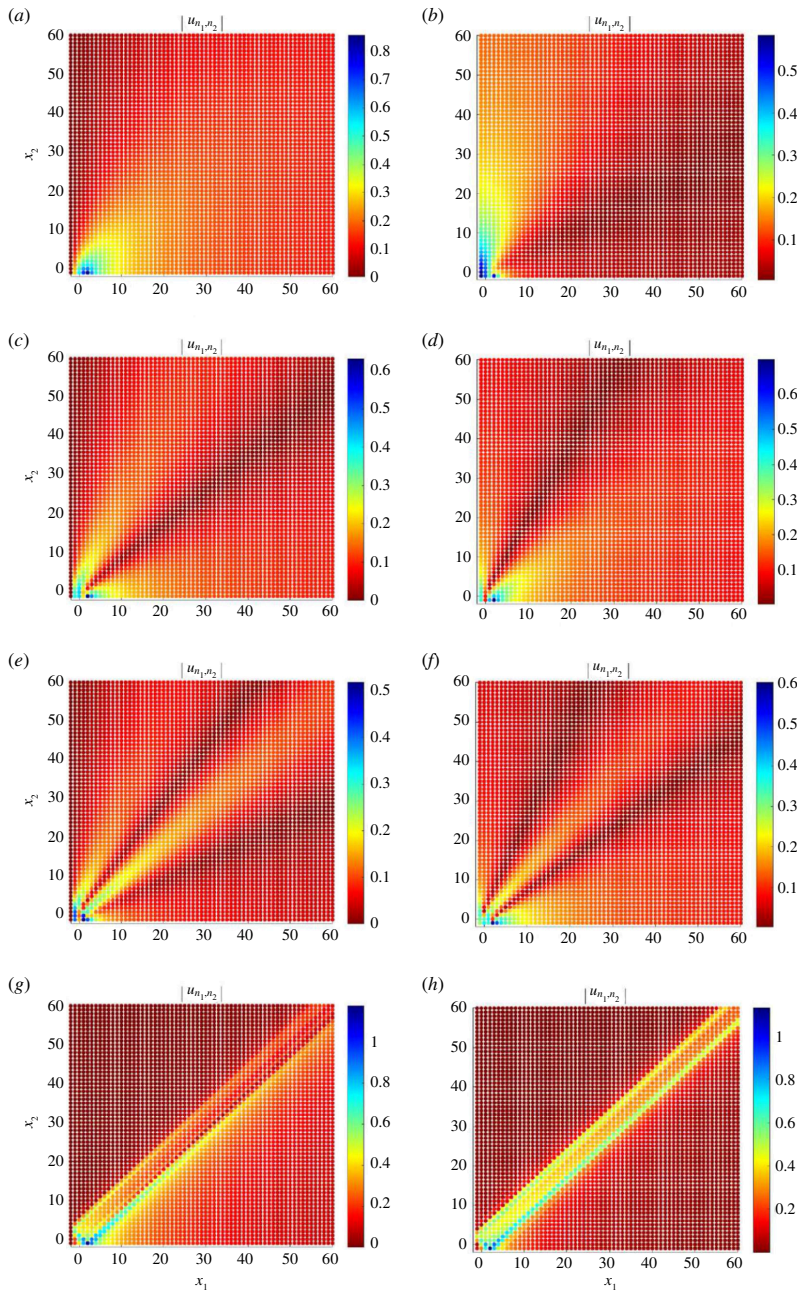
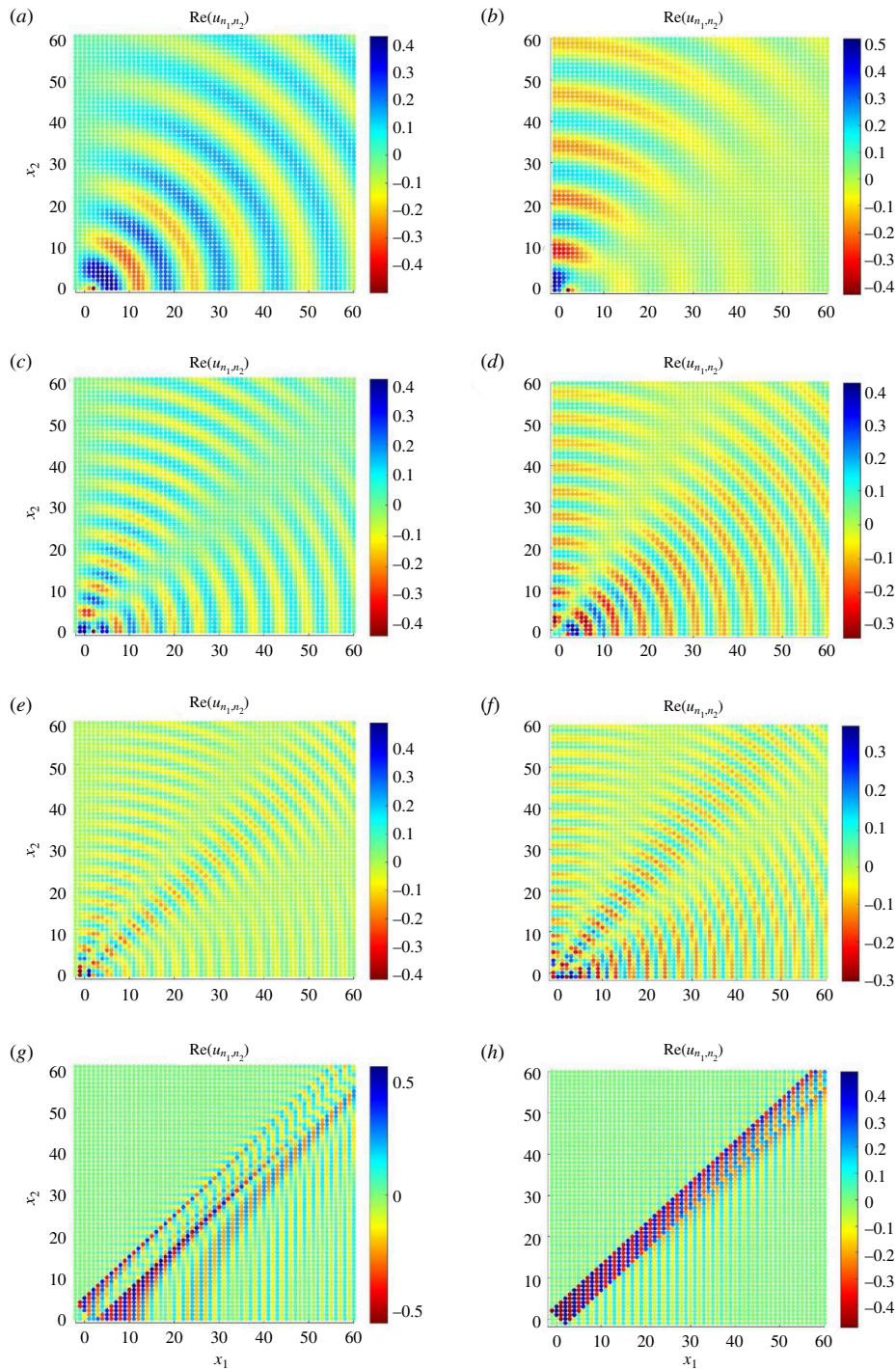**Figure 5.** Total displacements for the constrained quadrant, with a fixed vertical boundary (see (*a*), (*c*), (*e*) and (*g*)), and the free quadrant (see (*b*), (*d*), (*f*) and (*h*)) when subjected to a point force along their lateral boundaries at $x_1 = 2$. The loading frequency is taken as (*a, b*) $\omega_0 = 0.5$, (*c, d*) $\omega_0 = 1$, (*e, f*) $\omega_0 = 1.5$ and (*g, h*) $\omega_0 = 2$. The computations for the constrained quadrant are based on (5.11), (6.1) and (6.2), whereas those for the free quadrant have been computed with (7.10), (7.12) and (7.13).

displacement along the majority of these rays is higher than in the case of the quadrant with a fixed boundary, as expected on physical grounds.

19

royalsocietypublishing.org/journal/rspa Proc. R. Soc. A **480**: 20240099

Figure 6. Real part of the displacement fields for the constrained quadrant, with a fixed vertical boundary (see (a), (c), (e) and (g)), and the free quadrant (see (b), (d), (f) and (h)) when subjected to a point force along their lateral boundaries at $x_1 = 2$. The loading frequency is taken as (a, b) $\omega_0 = 0.5$, (c, d) $\omega_0 = 1$, (e, f) $\omega_0 = 1.5$ and (g, h) $\omega_0 = 2$. The computations for the constrained quadrant are based on (5.11), (6.1) and (6.2), whereas those for the free quadrant have been computed with (7.10), (7.12) and (7.13).

(b) Wave propagation in the quadrant

In addition, we note the computations in figure 5 do not indicate the behaviour of potential waveforms propagating in the medium. For this, one must consider the real or imaginary parts of the derived complex displacement amplitudes. These quantities exhibit oscillations and both carry an additional spatially dependent phase factor that modulates the amplitudes presented in figure 5. Wave patterns corresponding to the total displacement fields of figure 5 are shown in figure 6.

For low frequencies of the point load, the lattice sustains a response analogous to the corresponding continuum model [44], obtained when $\omega \to +0$. In this case, waves having circular wave fronts (see figure 6a,b) propagate outwardly from the free boundary's source. In particular, and in direct correspondence to the total displacements shown in figure 5a,b, the circular wave fronts have amplitudes that are modulated in the direction tangential to the wavefront. The amplitude of these waves is largest in those regions of the quadrant that undergo the highest total displacement which are attributed to the orientation of stress concentrations occurring at the quadrant's corner. This is also common feature of the remaining plots in figure 5.

Furthermore, when the frequency is increased, the wave fronts propagating in the medium assume almost elliptical wavefronts as we transition from a low-frequency regime with the isotropic dynamic response to one with strong anisotropy. Once more, the effect can linked to the slowness contours of the bulk system observed in figure 3. In particular, even in regimes where one would expect strong localization such as in the case of figure 6g,h, we still observe the presence of some small oscillations in the lattice outside of the localized deformations. For example, see above and below the highly localized wave form propagating at 45° measured from the x_1-axis in figure 6h. There it is apparent there are small oscillations in the structure which is consistent with the fact that at this frequency, the structure has slowness contours with some small curvature (see figure 3).

Finally, we mention that while the slowness contours may provide information about the topology of the waveforms propagating in the bulk lattice, they cannot predict the deformations these waveforms induce when interacting with the boundary of the quadrant. On the other hand, the analytical solution presented here, based on the application of the Wiener–Hopf technique, provides the information required to understand (i) how waves in the structure interact with abruptly changing boundaries and (ii) the phase and spatially varying amplitude of such waves in the time harmonic regime.

9. Conclusions

In the present article, we have considered two problems concerning the response of a lattice quadrant subjected to point load along its free lateral boundary, while the vertical boundary is fixed or free to move, with the intention of exploiting the method developed in [1] in the solution of such problems. The solution to these canonical problems has been developed using the discrete Fourier transform with respect to the principal lattice directions. This has led to the bulk lattice equations providing a transformed equation, involving two transform variables, incorporating knowledge of the boundary conditions and loading along the quadrant's free boundary. Utilizing the dispersion relation for wave motion in the lattice bulk, the transformed equation is then 'lifted' [1] to equations connecting only the boundary response of the system. This equation then enables one to determine a Wiener–Hopf problem involving the transformed displacements along the lateral boundary. After solving the Wiener–Hopf equation, we are then able to determine the entire lattice response.

The solutions for the considered problems have been implemented in numerical schemes and they have been used to determine the quadrant's response for a range of frequencies

and load positions. In each, the computations reveal how the waves generated by the point load propagate in the lattice, which may admit non-trivial topological features in frequency regimes where dynamic anisotropy is present. They also show how those waveforms interact with multiple lattice boundaries. An important feature of this investigation has involved the analysis of the high strains produced as a result of the loading near the corner point of the medium. These high strains occur in regions having a preferential direction within the bulk. At low frequencies, the corner of the lattice acts as a stress concentrator in the system, whereas in regimes with strong dynamic anisotropy this point appears to be relatively undisturbed with the majority of the dynamic response being concentrated in highly localized waveforms (e.g. see figures 5*g,h* and 6*g,h*).

In achieving the above analytical and numerical results, we have validated the theoretical technique developed in [1] to handle dynamic problems in stratified systems with abruptly changing geometries. We note the method adopted here has further extensions to a range of problems concerning structured systems having different geometries, mechanical responses (e.g. in-plane motions and flexural deformations) and a range of boundary conditions embedding numerous mechanical features (e.g. elastic supports, internal resonances and gyroscopic features). The work presented has applications in the analysis of structures commonly found in materials science and civil engineering, where an important paradigm in their study involves understanding their dynamic responses and wave scattering properties.

References

1. Kisil AV. 2024 A generalization of the Wiener–Hopf method for an equation in two variables with three unknown functions. *SIAM J. Appl. Math.* **84**, 464–476. (doi:10.1137/23M1562445)
2. Ali A, Mitra A, Aissa B. 2022 Metamaterials and metasurfaces: a review from the perspectives of materials. *Mech. Adv. Metadevices. Nanomater. (Basel)* **12**, 1027. (doi:10.3390/nano12061027)
3. Noble B. 1958 *Methods based on the wiener-hopf technique*. London: Pergamon Press.
4. Kisil AV, Abrahams ID, Mishuris G, Rogosin SV. 2021 The wiener–hopf technique, its generalizations and applications: constructive and approximate methods. *Proc. R. Soc. A.* **477**, 200210533. (doi:10.1098/rspa.2021.0533)
5. Sharma BL. 2015 Diffraction of waves on square lattice by semi-infinite crack. *SIAM J. Appl. Math.* **75**, 1171–1192. (doi:10.1137/140985093)
6. Bhat HS, Osting B. 2010 Diffraction on the two-dimensional square lattice. *SIAM J. Appl. Math.* **70**, 1389–1406. (doi:10.1137/080735345)

7. Sharma BL. 2015 Diffraction of waves on square lattice by semi-infinite rigid constraint. *Wave Motion* **59**, 52–68. (doi:10.1016/j.wavemoti.2015.07.008)

8. Sharma BL, Eremeyev VA. 2019 Wave transmission across surface interfaces in lattice structures. *Int. J. Eng. Sci.* **145**, 103173. (doi:10.1016/j.ijengsci.2019.103173)

9. Sharma BL. 2020 Transmission of waves across atomic step discontinuities in discrete nanoribbon structures. *Z. Angew. Math. Phys.* **71**, 73. (doi:10.1007/s00033-020-01294-9)

10. Maurya G, Sharma BL. 2019 Scattering by two staggered semi-infinite cracks on square lattice: an application of asymptotic Wiener–Hopf factorization. *Z. Angew. Math. Phys.* **70**, 133. (doi:10.1007/s00033-019-1183-2)

11. Medvedeva E, Assier R, Kisil A. 2024 Diffraction by a set of collinear cracks on a square lattice: an iterative Wiener–Hopf method. *Wave Motion* **129**, 103332. (doi:10.1016/j.wavemoti.2024.103332)

12. Sharma BL. 2022 Surface wave across crack-tip in a lattice model. *Phil. Trans. R. Soc. A* **380**, 20210396. (doi:10.1098/rsta.2021.0396)

13. Nieves MJ, Sharma BL. 2024 Interaction of in-plane waves with a structured penetrable line defect in an elastic lattice. *Int. J. Eng. Sci.* **197**, 104011. (doi:10.1016/j.ijengsci.2023.104011)

14. Slepyan LI, Troyankina LV. 1984 Fracture wave in a chain structure. *J. Appl. Mech. Tech. Phys.* **25**, 921–927. (doi:10.1007/BF00911671)

15. Slepyan LI. 2002 *Models and phenomena in fracture mechanics, foundations of engineering mechanics*. Heidelberg, Germany: Springer Berlin. (doi:10.1007/978-3-540-48010-5)

16. Marder M, Gross S. 1995 Origin of crack tip instabilities. *J. Mech. Phys. Solids* **43**, 1–48. (doi:10.1016/0022-5096(94)00060-I)

17. Mishuris GS, Movchan AB, Slepyan LI. 2007 Waves and fracture in an inhomogeneous lattice structure. *W. R. C. M.* **17**, 409–428. (doi:10.1080/17455030701459910)

18. Mishuris GS, Movchan AB, Slepyan LI. 2009 Localised knife waves in a structured interface. *J. Mech. Phys. Solids* **57**, 1958–1979. (doi:10.1016/j.jmps.2009.08.004)

19. Berinskii IE, Slepyan LI. 2017 How a dissimilar chain is splitting. *J. Mech. Phys. Solids* **107**, 509–524. (doi:10.1016/j.jmps.2017.07.014)

20. Gorbushin N, Mishuris G. 2019 Dynamic fracture of A dissimilar chain. *Philos. Trans. R. Soc.* **377**, 20190103. (doi:10.1098/rsta.2019.0103)

21. Piccolroaz A, Gorbushin N, Mishuris G, Nieves MJ. 2020 Dynamic phenomena and crack propagation in dissimilar elastic lattices. *Int. J. Eng. Sci.* **149**, 103208. (doi:10.1016/j.ijengsci.2019.103208)

22. Huang KX, Shui GS, Wang YZ, Wang YS. 2021 Enhanced fracture resistance induced by coupling multiple degrees of freedom in elastic wave metamaterials with local resonators. *J. Elast.* **144**, 33–53. (doi:10.1007/s10659-021-09825-9)

23. Carta G, Brun M. 2015 Bloch–floquet waves in flexural systems with continuous and discrete elements. *Mech. Mater.* **87**, 11–26. (doi:10.1016/j.mechmat.2015.03.004)

24. Kamotski IV, Smyshlyaev VP. 2019 Bandgaps in two-dimensional high-contrast periodic elastic beam lattice materials. *J. Mech. Phys. Solids* **123**, 292–304. (doi:10.1016/j.jmps.2018.08.024)

25. Brun M, Movchan AB, Slepyan LI. 2013 Transition wave in a supported heavy beam. *J. Mech. Phys. Solids* **61**, 2067–2085. (doi:10.1016/j.jmps.2013.05.004)

26. Brun M, Giaccu GF, Movchan AB, Slepyan LI. 2014 Transition wave in the collapse of the san saba bridge. *Front. Mater.* **1**, 12. (doi:10.3389/fmats.2014.00012)

27. Nieves MJ, Mishuris GS, Slepyan LI. 2016 Analysis of dynamic damage propagation in discrete beam structures. *Int. J. Solids Struct.* **97**, 699–713. (doi:10.1016/j.ijsolstr.2016.02.033)

28. Craster RV, Kaplunov J, Pichugin AV. 2010 High-frequency homogenization for periodic media. *Proc. R. Soc. A.* **466**, 2341–2362. (doi:10.1098/rspa.2009.0612)

29. Nolde E, Craster RV, Kaplunov J. 2011 High frequency homogenization for structural mechanics. *J. Mech. Phys. Solids* **59**, 651–671. (doi:10.1016/j.jmps.2010.12.004)

30. Martin PA. 2006 Discrete scattering theory: green's function for a square lattice. *Wave Motion* **43**, 619–629. (doi:10.1016/j.wavemoti.2006.05.006)

31. Garau M, Carta G, Nieves MJ, Jones IS, Movchan NV, Movchan AB. 2018 Interfacial waveforms in chiral lattices with gyroscopic spinners. *Proc. R. Soc. Ser. A* **474**, 20180132. (doi:10.1098/rspa.2018.0132)

32. Nieves MJ, Carta G, Pagneux V, Brun M. 2020 Rayleigh waves in micro-structured elastic systems: non-reciprocity and energy symmetry breaking. *Int. J. Eng. Sci.* **156**, 103365. (doi:10.1016/j.ijengsci.2020.103365)

33. Nieves MJ, Carta G, Pagneux V, Brun M. 2021 Directional control of rayleigh wave propagation in an elastic lattice by gyroscopic effects. *Front. Mater.* **7**, 602960. (doi:10.3389/fmats.2020.602960)

34. Carta G, Nieves MJ, Brun M. 2022 Unidirectional interfacial waves in gyroscopic elastic systems. In *10th Int. Conf. on Wave Mechanics and Vibrations 4th-6th*. Lisbon, Portugal: Springer. (doi:10.1007/978-3-031-15758-5_117)

35. Carta G, Nieves MJ, Brun M. 2023 Forcing the silence of the lamb waves: uni-directional propagation in structured gyro-elastic strips and networks. *Eur. J. Mech. A Solid.* **101**, 105070. (doi:10.1016/j.euromechsol.2023.105070)

36. Shanin AV, Korolkov AI. 2022 Diffraction by a dirichlet right angle on a discrete planar lattice. *Quart. Appl. Math.* **80**, 277–315. (doi:10.1090/qam/1612)

37. Nieves MJ, Movchan AB. 2022 Meso-scale method of asymptotic analysis of elastic vibrations in periodic and non-periodic multi-structures. *Q. J. Mech. Appl. Math.* **75**, 171–214. (doi:10.1093/qjmam/hbac011)

38. Ganesh M, Hawkins SC. 2015 An efficient algorithm for computing acoustic wave interactions in large -obstacle three dimensional configurations. *BIT Numer. Math.* **55**, 117–139. (doi:10.1007/s10543-014-0491-3)

39. Ganesh M, Hawkins SC. 2019 A fast high order algorithm for multiple scattering from large sound-hard three dimensional configurations. *J. Comput. Appl. Math.* **362**, 324–340. (doi:10.1016/j.cam.2018.10.053)

40. Martin PA. 2006 *Multiple scattering: interaction of time-harmonic waves with N obstacles, encyclopedia of mathematics and its applications (no.107)*. Cambridge, UK: Cambridge University Press.

41. Nieves MJ, Kisil A, Mishuris G. 2024 Data from: Analytical and numerical study of anti-plane elastic wave scattering in a structured quadrant subjected to a boundary point load. Figshare. (doi:10.6084/m9.figshare.c.7396508)

42. Sheremet VD. 2002 *Handbook on green's functions and matrices*. Southampton, UK: WIT Press / Computational Mechanics.

43. Cadet S. 1989 Propagation and interactions of nonlinear shear waves in a discrete lattice. *Wave Motion* **11**, 77–97. (doi:10.1016/0165-2125(89)90014-0)

44. Forsythe GE, Wasow RW. 1960 *Finite-difference methods for partial differential equations, applied mathematics series*, p. 444. New York, NY: John Wiley & Sons, Inc.